



Carbon flux from bio-optical profiling floats: Calibrating transmissometers for use as optical sediment traps



Meg Estapa^{a,*}, Colleen Durkin^{b,1}, Ken Buesseler^b, Rod Johnson^c, Melanie Feen^a

^a Department of Geosciences, Skidmore College, Saratoga Springs, NY, USA

^b Marine Chemistry and Geochemistry, Woods Hole Oceanographic Institution, Woods Hole, MA, USA

^c Bermuda Institute of Ocean Sciences, St. George's, GE01, Bermuda

ARTICLE INFO

Keywords:

Biological pump

Carbon flux

BATS

Neutrally-Buoyant Sediment Trap

Optical sediment trap

ABSTRACT

Our mechanistic understanding of the processes controlling the ocean's biological pump is limited, in part, by our lack of observational data at appropriate timescales. The “optical sediment trap” (OST) technique utilizes a transmissometer on a quasi-Lagrangian platform to collect sedimenting particles. This method could help fill the observational gap by providing autonomous measurements of particulate carbon (PC) flux in the upper mesopelagic ocean at high spatiotemporal resolution. Here, we used a combination of field measurements and laboratory experiments to test hydrodynamic and zooplankton-swimmer effects on the OST method, and we quantitatively calibrated this method against PC flux measured directly in same-platform, neutrally buoyant sediment traps (NBSTs) during 5 monthly cruises at the Bermuda Atlantic Time-series Study (BATS) site. We found a well-correlated, positive relationship ($R^2=0.66$, $n=15$) between the OST proxy, and the PC flux measured directly using NBSTs. Laboratory tests showed that scattering of light from multiple particles between the source and detector was unlikely to affect OST proxy results. We found that the carbon-specific attenuation of sinking particles was larger than literature values for smaller, suspended particles in the ocean, and consistent with variable carbon: size relationships reported in the literature for sinking particles. We also found evidence for variability in PC flux at high spatiotemporal resolution. Our results are consistent with the literature on particle carbon content and optical properties in the ocean, and support more widespread use of the OST proxy, with proper site-specific and platform-specific calibration, to better understand variability in the ocean biological pump.

1. Introduction

The biological pump is a critical system of processes controlling the ocean's ability to take up carbon dioxide from the atmosphere and sequester it in deep water (Volk and Hoffert, 1985). Briefly, the process is as follows: 1) Autotrophic organisms in the euphotic zone fix CO_2 , creating organic matter; 2) if this organic matter is not respired back to CO_2 throughout the food web within the euphotic zone, it is exported out of the euphotic zone; and 3) it is sequestered beneath the permanent thermocline. Heterotrophic respiration of organic matter in the mesopelagic (top 1 km of the ocean) below the euphotic zone further reduces the amount of exported organic matter, but the small fraction that escapes represents an important flux term in the long-term carbon cycle.

Mechanisms by which organic matter is exported from the surface ocean include gravitational settling of particulate organic matter

(Turner 2015), active transport of organic matter by vertically-migrating zooplankton that feed at the surface but respire and defecate at depth (Steinberg et al., 2000), and the physical subduction of organic matter (Levy et al., 2013; Omand et al., 2015). Gravitational settling of particulate organic matter, a major contributor to export flux and the sub-process of interest in this study, includes the direct export of aggregated autotrophic biomass, for instance at the termination of the North Atlantic Spring Bloom (Martin et al., 2011), the rapid settling of zooplankton fecal pellets (Turner, 2002), and the slower settling of unaggregated, small detrital particles (Alonso-Gonzalez et al., 2010; Durkin et al., 2015). We currently lack a mechanistic understanding of these export processes that is detailed enough to include in global climate models (Siegel et al., 2014). Contributing factors to this issue are a lack of observational data at appropriate spatiotemporal scales and a lack of observational coverage throughout the global oceans (Bishop, 2009).

* Corresponding author.

E-mail address: mestapa@skidmore.edu (M. Estapa).

¹ Present address: Moss Landing Marine Labs, Moss Landing, CA, 95039, USA.

1.1. Methods for observing the biological carbon pump

Traditional methods for measurement of settling, particulate organic matter in the upper 1 km of the open ocean include radiochemical tracers and sediment trapping (Buesseler et al., 2007). All of the methods have specific advantages and disadvantages which are beyond the scope of this discussion, however they have in common the drawback that they are labor-intensive and require ship support. These traditional methods thus complicate our efforts to increase the number and spatiotemporal resolution of carbon flux observations in the upper mesopelagic.

In the last several years, increasing efforts have gone into development of methods for observing particulate organic matter flux that are deployable over long time periods from autonomous platforms such as profiling floats and gliders (Bishop et al., 2004, 2016; Bishop, 2009; Bishop and Wood, 2009; Briggs et al., 2011; Estapa et al., 2013; Dall'Olmo and Mork, 2014; Jackson et al., 2015). Briggs et al. (2011) observed during the 2008 North Atlantic Bloom Experiment that large, settling organic particles such as phytoplankton aggregates generated “spikes” in unfiltered data from optical backscattering, beam attenuation, and fluorescence sensors deployed on a variety of platforms. They were able to relate this spike signal to carbon flux by large particles because the leading edge of the sinking bloom particle population was visible in a series of profiles collected over many weeks in a single water parcel. The advantage of this method is that the physical capture of particles is not required (thereby avoiding hydrodynamic effects), but the method is insensitive to particles too small to manifest as optical spikes.

Dall'Olmo and Mork (2014) used an annual cycle of backscattering profiles from a profiling float in a confined basin to track the depth-integrated accumulation of POC in the water column, from which they were able to derive the long-term carbon export. Like the method of Briggs et al. (2011), this technique has the advantage of not requiring the physical collection of settling particles. However, this method may be biased by other POC gain and loss processes, and it is not sensitive to flux via large, rare particles unless they disaggregate into the size range where the backscattering measurement is most sensitive (order 0.2–20 μm ; Dall'Olmo and Mork, 2014).

Methods based on changes in the vertical distribution of backscattering in consecutive profiles (Briggs et al., 2011; Dall'Olmo and Mork, 2014; Jackson et al., 2015) may also miss rapidly-settling particles, if the profile repeat interval is long or the profiling depth is shallow (Jackson et al., 2015). They may also be impacted by horizontal advection or spatial heterogeneity of sinking particles. Finally, these methods cannot measure particle fluxes under steady state conditions (Dall'Olmo and Mork, 2014), because the estimate is derived from rates of change of vertical backscattering profiles or other optical particle measurements.

1.2. Optical sediment trap technique

Several researchers have used transmissometers mounted vertically on profiling floats drifting at depth to physically intercept settling particles on the upward-facing optical window covering the detector (Bishop et al., 2004; Bishop, 2009; Bishop and Wood, 2009; Estapa et al., 2013). Bishop et al. (2016) have also recently developed a related method that images settling particles at high temporal resolution with a camera looking upward at the base of a sediment trap, rather than by using a transmissometer. The transmissometer-based method was originally pioneered by Bishop et al. (2004) in a long term iron-fertilization study in the Southern Ocean, rendering accessible a region where it was previously difficult to make long-term carbon flux measurements. In this method, the rate of change of attenuation (for a transmissometer, equivalent to beam attenuation coefficient multiplied by pathlength) while the platform drifts at depth serves as a particle flux proxy. Here, we refer to this technique generically as the

“optical sediment trap” (OST) method. Different implementations of the transmissometer-based OST method have so far involved increasing the sampling interval to 1 h or 15 min to better observe variability in flux and avoid artifacts (Estapa et al., 2013); changes in WETLabs transmissometer window design, which to our knowledge have not affected the quality of reported data (the older CRV-5 optical windows were flush with the pressure housing; the newer CRV-2000 windows are raised slightly to allow insertion of a flow tube during pre-deployment calibration); and measurement of attenuation flux relative to the start of the drift phase (Estapa et al., 2013) vs. after a window-rinsing operation at the end of the drift phase (Bishop et al., 2004; Bishop, 2009; Bishop and Wood, 2009). The latter implementation method could result in an underestimate of flux if window-rinsing is not completely effective, as suggested by data in Estapa et al. (2013).

The OST method, whether implemented with an imaging trap or transmissometer, has three advantages relative to the methods based on temporal changes in profiles of optical backscattering described above: 1) it should be sensitive to both small and most large particles (Estapa et al., 2013), 2) it does not require a long timeseries of profiles at high time-resolution following a single water parcel to make a flux measurement, and 3) it works when particle fluxes through a depth horizon are constant during the elapsed time between profiles. The transmissometer-based OST method additionally can be implemented using commercially-available platforms and sensors. The main disadvantages of OST measurements are that they have not yet been compared directly with other methods of estimating carbon flux, and they may be subject to potential hydrodynamic and swimmer effects (similar to those affecting traditional sediment traps; Buesseler et al., 2007). In this study, we use a combination of field observations and laboratory experimentation to address these issues.

2. Methods

2.1. Study site and deployment design

We made particle flux measurements using the OST method during a series of five short cruises (see Table 1 for dates and deployment locations) in conjunction with the Bermuda Atlantic Time-series Study (BATS; Lomas et al., 2013). The sensors used as OSTs were all 25 cm pathlength, near-neutrally buoyant, 650 nm transmissometers with 0.9° acceptance angles, beam divergence angles around 0.3°, and nominal, 7.6 mm beam diameters (C-Rover 2000, WETLabs, Inc.; www.wetlabs.com/c-rover-2000; Fig. 1) deployed with the detector window facing upwards as described by Bishop et al. (2004) and Bishop and Wood (2009). Unlike in Bishop's studies, we did not use outflow from pumped sensors to “rinse” the C-Rover window to avoid introducing complexity to the salinity sensor's flow path, and because Estapa et al. (2013) found that rinsing had no effect on the rate of sensor drift in paired deployments of rinsed and non-rinsed floats. Additionally, deployments reported here were short enough to preclude appreciable sensor drift. We deployed transmissometers each month on a group of 4–5 neutrally-buoyant, drifting platforms, which were recovered at the end of each cruise. Each set of deployments lasted 1.5–3 days. Platforms included three neutrally-buoyant sediment traps (NBSTs, Valdes and Price, 2000) and 1 or 2 profiling floats (Navis BGCi, Seabird Scientific). The NBST platforms are constructed around Sounding Oceanographic Lagrangian Observer (SOLO) profiling floats and also carried four sediment trap tubes (Fig. 1, left). The Navis profiling floats carried CTDs, O₂ optodes, backscattering (700 nm), fluorescence (chlorophyll, colored dissolved organic matter), and tilt sensors, in addition to the transmissometer (Fig. 1, right).

NBSTs were programmed to descend to a single measurement depth (150, 200, 300 or 500 m), sample for a preprogrammed 2–3 d period, and then ascend to the surface for recovery. NBSTs operated as in prior studies (Lamborg et al., 2008; Owens et al., 2013) except we added transmissometers and improved trap tube lid closure mechan-

Table 1
Summary of NBST deployments.

Deployment date	Depth	Deployment location	Deployment length (d)	PC flux replicates	PC flux (\pm s.d. or range, mg-C m ⁻² d ⁻¹)				
					NBST	PITs	PSD slope ^A		
5 July 2013	150	31.7°N, 64.2°W	2.92	3	20.9 \pm 7.6 ^B	13.9 \pm 4.4	3.4		
	300		2.86	3	9.0 \pm 1.4 ^B			5.24 \pm 0.70	3.8
1 Aug 2013	150	31.6°N, 64.2°W	2.45	2	21.5 \pm 1.8	11.9 \pm 6.0	3.5		
	200		2.48	2	12.9 \pm 1.7			8.2 \pm 2.8	2.9
	300		2.42	3	7.1 \pm 1.4			6.4	4.0
17 Sept 2013	150	31.7°N, 64.1°W	2.69	3	12.2 \pm 2.5	13.67 \pm 0.30	3.1		
	300		2.67	3	6.6 \pm 2.6			5.26	3.4
	500		2.70	3	7.8 \pm 1.4				3.8
19 Oct 2013	150	31.7°N, 64.2°W	2.65	3	10.6 \pm 2.9	5.1 \pm 2.3	3.2		
	300		2.63	2	1.3 \pm 3.8			3.68 \pm 0.8	3.2
	500		2.64	3	5.2 \pm 3.4				3.5
4 March 2014	150	31.6°N, 64.2°W	1.47	3	13.7 \pm 4.2	26.2 \pm 1.1	3.2		
	300		1.48	3	11.0 \pm 2.3			15.0 \pm 5.5	3.4
	500		1.45	2	11.6 \pm 4.7				3.6

^A PSD slopes from Durkin et al. (2015).

^B Absolute flux values should be treated with caution due to platform vertical motions.

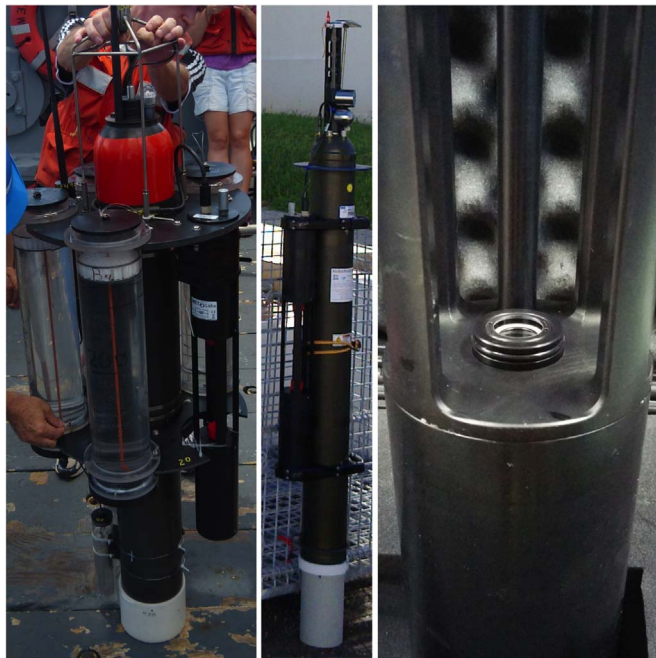


Fig. 1. Left panel: Neutrally-buoyant sediment trap (NBST) carrying 4 sediment trap tubes and an integrated C-Rover transmissometer (WETLabs C-Rover 6b). Center panel: Navis BGCi profiling float (Seabird Scientific) also carrying a C-Rover transmissometer (WETLabs C-Rover 2 K, identical in size and optical specifications to the C-Rover 6b). Right panel: Close-up photograph of the lower optical window of the C-Rover 2 K.

Table 2
Summary of Navis float deployments.

Deployment date	Park depth range (m)	Deployment location	Number of floats	Number of flux measurements	Notes
5 July 2013	30–217	31.7°N, 64.2°W	2	2	A, B
1 Aug 2013	133–906	31.6°N, 64.2°W	2	13	C
17 Sept 2013	110, 292	31.7°N, 64.1°W	1	1	B
19 Oct 2013	134, 380	31.7°N, 64.2°W	1	1	B
4 March 2014	490, 425	31.6°N, 64.2°W	1	1	A

^A First deployment after service/ballast change, target depths not reached on first few profiles.

^B Firmware error; no upper water column data on some profiles.

^C Floats continued to profile for 8 days after deployment.

isms. During the July 2013 deployment the NBSTs were programmed to hold depth within ± 25 m of the measurement depth, while in subsequent deployments this band was narrowed to ± 10 m. Navis floats first completed an initial down-and-up dive without parking, then parked and collected a flux measurement at 1 or 2 consecutive depths within the 2–3 d deployment period with a profile ascent in between. A float firmware error early in the fieldwork period prevented collection of upper water column data in some of the profiles, although this was remedied by the end of the field season. To examine the general hydrographic setting during each cruise, water-column profile data were averaged in density space for each cruise from the available float profile data. Transmissometers on all platforms sampled at 15 min intervals during the platform drift phase. The deployment times, locations, and target depths during the 5 cruises are summarized for NBSTs in Table 1 and for Navis floats in Table 2.

2.2. OST data analysis

The OST method uses the rate of change of particle attenuation at 650 nm ($ATN(650)$), measured from a quasi-Lagrangian, profiling float drifting at depth (i.e., the “park phase” in the Argo float profiling sequence). Attenuance is defined as $-\ln(\text{signal}/\text{reference})$, where *signal* is the light intensity at the transmissometer detector and *reference* is the source intensity. When measured with a transmissometer, ATN is equal to the product of the beam attenuation (c), defined operationally here as $c = -\ln(\text{signal}/\text{reference})/\text{pathlength}$, and the transmissometer pathlength. While attenuation is unitless, we can also think of it as the total attenuation cross section (σ_e , units of m²; Mobley, 1994) of particles deposited within the transmissometer beam

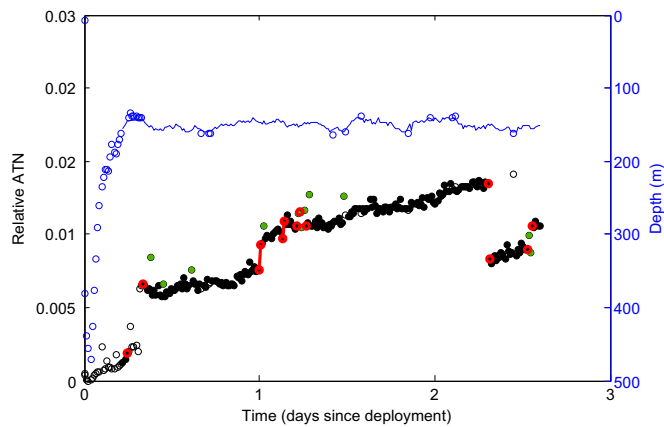


Fig. 2. Example illustrating raw data collected every 15 min from transmissometer during NBST drift phase (October 2013, 150 m). Blue line (right y-axis) shows NBST depth when it was within 10 m of the target pressure, while blue circles show out-of-depth points. Open black circles (left y-axis) show corresponding attenuation data excluded from analysis. Green dots show spikes excluded from the flux proxy but counted for comparison to gel-trap swimmers. Red circles show endpoints of jumps. Positive jumps not interrupted by spikes or out-of-depth points (red circles connected by lines) were also considered as part of the flux proxy. The increase of ATN over time is due to the accumulation of particles on the upward-looking window of the transmissometer. The OST flux proxy has two components: the average rate of change in the slowly-increasing signal (black dots) and the positive-jump increase (red circles connected by lines) normalized to the deployment length. See Supplementary Information, Figs. S1–S3 for data from other float and NBST deployments during this study. (For interpretation of the references to color in this figure legend, the reader is referred to the web version of this article.)

area (units m^2), and therefore we refer to it here with units of $\text{m}^2 \text{m}^{-2}$. Fig. 2 shows an example of unprocessed attenuation data and illustrates the data processing steps. The OST flux proxy computation used here has been described in detail by Estapa et al. (2013), but has been adjusted to account for the higher sampling frequency in this study (every 15 min instead of 1 h), and is now reported in units of attenuation rather than beam attenuation. To summarize, we first excluded data points when the platform was not sampling within 10 m of its measurement depth. Next, we used a median filter to remove spikes from the raw signal, and interpolated over the resulting data gaps. In the next step, we identified jumps by finding spikes in the absolute magnitude of the first difference of the de-spiked timeseries. The dynamic jump threshold was set as the maximum of either $0.001 \text{ m}^2 \text{m}^{-2}$ between consecutive 15 min observations (3 times the instrument noise), or the 95th percentile of absolute first differences. The ATN timeseries was then divided into segments at jump points, and segments further subdivided into 12-point (3-h) fitting windows over which the rate of change of ATN was computed using Type I linear regression. The rate of change of ATN (i.e., the slope of the best fit line to ATN vs. time) serves as the proxy for particulate carbon flux.

Additionally, we examined the effect of including positive jumps in the ATN vs. time signal that did not encompass spikes or out-of-depth points when the platform may have been making active ballast adjustments (Fig. 2), as a component of the flux proxy (the “discontinuous flux component” described by Estapa et al. (2013)). To do this, we normalized the cumulative, positive jump signal in each drift phase to the length of the drift phase.

Finally, we considered the implications of horizontal shielding and vertical shading of the upward-facing transmissometer window by the adjacent platform and upper part of the transmissometer housing. “Vertical shading” arises due to the fact that particles cannot settle directly downward onto the transmissometer window but must be carried in from the side by ambient turbulent motions. For the Navis-mounted OSTs, vertical shading was due only to the upper housing of the transmissometer, while the NBST-mounted OSTs may also have been shaded by the upper trap tube support plate (Fig. 1). “Horizontal

shielding” arises from the fact that the transmissometer path is not equally open on all sides due to the adjacent float body and, in the case of the NBST, sediment trap tubes. Transmissometers on NBSTs in this study were 56% shielded from the side, while transmissometers on Navis floats were 39% shielded. The difference is primarily due to the presence of trap tubes on the NBST, and the greater diameter of the SOLO float relative to the Navis float (Fig. 1).

Here, we have extended the analysis of Estapa et al. (2013) to consider a broader range of turbulent dissipation rates that are more characteristic of the upper mesopelagic (Waterhouse et al., 2014) and we have taken into account the specific impacts of shielding on particles with a range of settling velocities. The analysis indicated that in this study, shading and shielding corrections would be more likely to introduce bias than to remove it, so no corrections were performed. This analysis is discussed further, below (see Section 4.3).

2.3. Sediment trap sample collection and analysis

We also used NBSTs to directly measure particulate carbon flux. Details are described fully in Durkin et al. (2015) but are summarized here. To preserve settling particulate matter for carbon analysis, 500 mL of formalin-poisoned brine solution was layered at the bottom of three trap tubes on each NBST that were filled with filtered seawater from beneath the mixed layer. A fourth tube on each NBST was loaded with a polyacrylamide gel trap insert (Ebersbach and Trull, 2008; McDonnell and Buesseler, 2010, 2012; Durkin et al., 2015) which preserved sizes and shapes of settled particles. The gel trap tube was then filled with filtered seawater. All tubes had areas of 0.0113 m^2 . After trap recovery, the upper seawater layer was siphoned off each tube, and the lower brine layer was drained through a $350 \mu\text{m}$ screen to separate the sinking fraction analyzed here from zooplankton presumed to have actively entered the trap (Lamborg et al., 2008; Owens et al., 2013). Owens et al. (2013) found no significant difference between wet-picked and screened trap samples collected over multiple seasons at BATS, however this may not be the case in all settings. In all trap tubes, brine layer salinities confirmed that the density interface remained intact during deployment. The $< 350 \mu\text{m}$ fractions were filtered onto precombusted GF/F filters (Whatman), immediately frozen, dried overnight at $45 \pm 5 \text{ }^\circ\text{C}$ on shore, and finally analyzed for total particulate carbon (PC) content via combustion elemental analysis (note that PIC fluxes at the BATS site are typically low, on average 5% of total carbon at 150 m; Owens et al., 2013). One PC measurement was made per trap tube. Occasionally single tube samples were compromised during collection or analysis. Reported NBST fluxes have a 5-cruise mean process blank value subtracted, and are the mean of 2 or 3 tubes (Table 1). Reported PC flux uncertainties are propagated from the standard deviation of the process blanks from the 5 cruises, and the standard deviation or range of the 2 or 3 PC measurements per NBST deployment.

All platforms were deployed in parallel with the standard surface-tethered BATS sediment trap array which has particle interceptor traps (PITs) at 150 m, 200 m, and 300 m (Knap et al., 1997). Carbon flux measurements collected as part of the time series program are reported alongside our NBST measurements. BATS protocols for collection and analysis of carbon flux samples are described in Knap et al. (1997), and compared in detail to NBST protocols by Owens et al. (2013). An additional modification from Knap et al. (1997) was the subtraction of a PIT carbon process blank, collected and processed as detailed in Owens et al. (2013). Values reported in Table 1 are means and standard deviations of multiple tubes (no standard deviation is reported when only one tube was available as in some samples). Sea surface height anomalies in the study area were obtained from objectively-analyzed satellite altimeter tracks (Collecte Localis Satellites, AVISO, <http://www.aviso.oceanobs.com>), separated in space (up to 100–200 km) and time (± 3 days) from the location and day of platform deployment.

The fourth trap tube containing a polyacrylamide gel on each NBST

was drained and the gel insert carefully removed and stored at 4 °C until analysis. A series of photomicrographs were taken of each gel trap at 7×, 16×, and 64× magnifications, and particles were enumerated and sized (Durkin et al., 2015). Power-law particle size distributions (PSDs) were computed for each gel trap from particle counts composited from images with different magnifications (Table 1; Durkin et al., 2015). The modeled, power law PSDs were used to estimate the uncertainty in the OST attenuation flux, and to estimate the total particle cross-sectional area flux to the traps. Recognizable zooplankton, presumed to have actively entered the gel traps, were also counted which we use here to quantify swimmer fluxes.

2.4. Laboratory experiments

Laboratory experiments were designed to characterize the effects of multiple scattering (defined below) on the OST flux proxy as particles accumulate on the transmissometer window, and to assess the natural variability in the optical properties of settling particles, which depend on particle size, shape, and composition. The phenomenon we refer to as “multiple scattering” occurs in bulk optical measurements at high particle concentrations, when light scatters off multiple particles before being detected (e.g., Kiefer and Soohoo, 1982). If it occurred in our application, it would cause the OST proxy signal to respond nonlinearly at high particle accumulations. We conducted multiple scattering tests using size-calibrated, polystyrene beads (Polybead, Inc.) ranging from 25 to 250 μm in size. Beads were suspended in distilled water at a range of concentrations and were gravity fed into a vertically oriented C-Rover equipped with a flow tube, which encloses the optical sampling volume for benchtop measurements. Data were collected for 1–2 min, the flow was stopped and beads were allowed to completely settle (evidenced by stabilization of the signal), and the final beam attenuation was recorded. Settling times varied depending on size, and were verified empirically in advance of experiments since the flow tube is opaque. Bead suspension mass concentration was determined by filtering aliquots in triplicate onto pre-weighed, 0.2 μm polycarbonate filters (Nucleopore), which were then dried and weighed until stable masses were achieved.

Similar experiments were conducted using natural particle assemblages chosen to mimic settling particles in the ocean. Natural particles consisted of dead cultures of *Thalassiosira weissflogii* (Reed Mariculture, Inc.), and surface plankton samples collected in less than 10 m of water from Iselin Pier, Woods Hole, MA, USA, and Saratoga Lake in Saratoga Springs, NY, USA. These samples were pre-settled overnight to remove non- or slowly-sinking particles. Experiments were carried out by immersing the C-Rover in a narrow, vertical tank filled so that the suspension would be even with the top of the beam-path, to eliminate small, organic particle adhesion to flow tube walls. Particles were fully resuspended in the tank prior to immersing the C-Rover. Suspension aliquots were collected separately to determine mass and PC concentrations, following methods described above.

3. Results

3.1. Field observations

During all cruises, the relative drift trajectories of the individual NBST, PITs, and Navis platforms were similar, with mean separation distances ranging from 1.6 to 10 km. These trajectories were consistent with the immediate mesoscale eddy field, which was visible in satellite altimetry measurements of the area (Fig. 3). The various platforms, deployed approximately 1 km apart, usually diverged from one another as they drifted. When the Navis platforms were deeper than tens of meters below the surface, average tilts were less than 1° (±0.2°). NBSTs were not equipped with tilt sensors but were commonly observed to sit upright in the water even at the surface. During the July 2013 deployment, ballasting errors and the ±25 m target depth

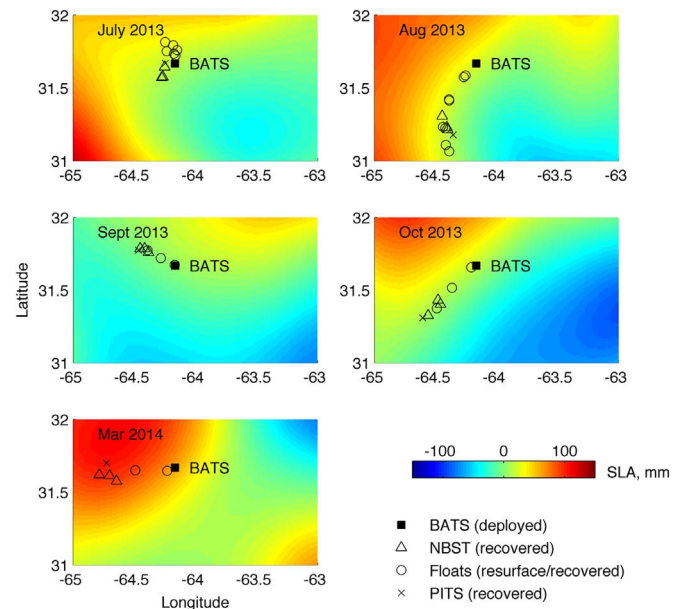


Fig. 3. Float, NBST, and PITs drift paths and sea-level anomalies near the BATS site during the cruises. SLA fields are based on objectively-analyzed satellite altimeter tracks separated in space (up to 100–200 km) and in time (± 3 days) from the day of platform deployment. The deployment location at the BATS site is denoted by the filled square. Open circles show the surfacing and final recovery locations of the floats, open triangles show the recovery locations of the NBSTs, and crosses show the recovery locations of the PITs array. In all cruises, the drift patterns of the platforms (deployed approximately 1 km apart at the BATS site) were fairly consistent with the inferred mesoscale circulation. The low SLA to the SE of the BATS site for the July–October 2013 cruises shows a cyclonic feature that persisted through the four month period.

window resulted in a downward drift of the NBSTs in between active buoyancy adjustments (Fig. S1) and thus absolute carbon fluxes should be interpreted with caution. However, same-platform OST and NBST observations should be comparable.

Mixed layer depths were determined from potential density profiles using a difference criterion of $\sigma_{\theta} = +0.125 \text{ kg m}^{-3}$ from the surface density. Mixed layer depths were generally shallower than 30 m during the July–October 2013 cruises, and around 170 m during the March 2014 cruise (Fig. 4). The chlorophyll fluorescence maximum shoaled from 125 m in July to 100 m in October. The March 2014 fluorescence signal was homogeneous throughout the upper 100 m (Fig. 4). A shallow O_2 maximum present between 50 and 70 m during the summer–fall stratified period had mixed out by the March cruise. In March, a local O_2 minimum was present and centered at 225 m.

PC fluxes to the NBSTs and PITs were generally highest at 150 m (the shallowest depth sampled) and decreased with depth (Table 1, Fig. 5). For the NBST observations, both shallow PC fluxes and flux attenuation were highest during July and August 2013. Fluxes to the NBSTs at 150 m ranged from $10.6 (\pm 2.9) \text{ mg-C m}^{-2} \text{ d}^{-1}$ in Oct 2013 to $21.5 (\pm 1.8) \text{ mg-C m}^{-2} \text{ d}^{-1}$ in August 2013 (values in parentheses are standard deviations; Table 1, Fig. 5). Transfer efficiencies measured with the NBSTs, defined here as the ratio of flux at 300 m to flux at 150 m, ranged from a low of 0.33 in August 2013 to a high of 0.85 in March 2014 (Table 1). Differences between fluxes to the PITs and NBSTs were sometimes positive and sometimes negative (Table 1). With the exception of the 300 m October samples, PC fluxes averages in the PITs array were within a factor of 2.2 of fluxes to the NBSTs, consistent with interplatform variability observed by Owens et al. (2013) during paired NBST deployments at the BATS site over a three year period. The 300 m October PITs sample was approximately 2.8 times the flux to the NBST (Table 1).

At 3 h time resolution, OST flux proxy values on the NBSTs ranged from zero to a high of $0.019 \text{ m}^2 \text{ m}^{-2} \text{ d}^{-1}$ (Fig. 5). At this time resolution, depth-attenuation trends in the OST proxy were not apparent, although

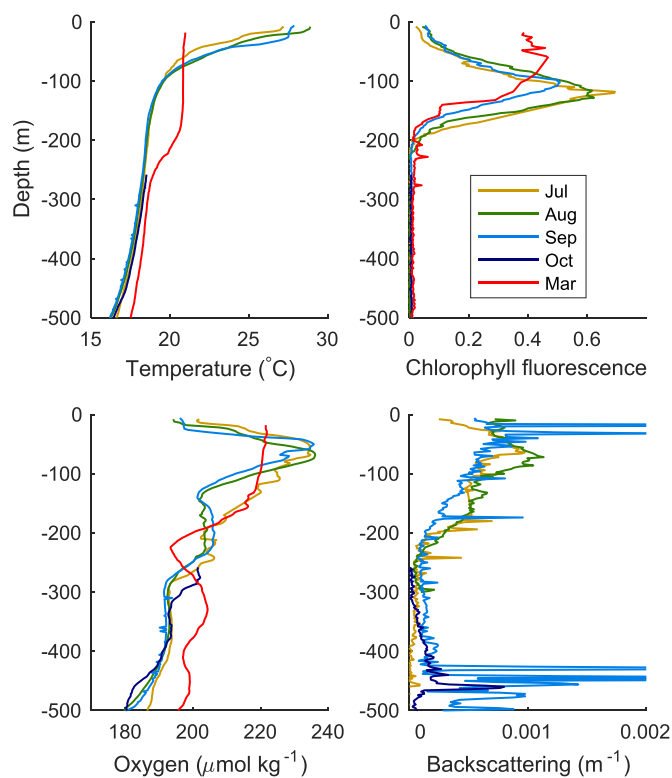


Fig. 4. Summary of water column properties during each of the 5 cruises. All float profiles were averaged in density space to create the plots. Top left panel: Temperature ($^{\circ}\text{C}$). Top right panel: Chlorophyll fluorescence (uncalibrated). Lower left panel: Dissolved oxygen ($\mu\text{mol kg}^{-1}$, uncalibrated). Lower right panel: Backscattering (700 nm) (m^{-1}). Colors denote month of each cruise. (For interpretation of the references to color in this figure legend, the reader is referred to the web version of this article.)

variance over time in the OST proxy decreased with depth. When averaged over entire 1.5–2.9 d deployment periods, the OST flux proxy ranged from 0.002 to 0.008 $\text{m}^2 \text{m}^{-2} \text{d}^{-1}$. At the longer 1.5–2.9 d timescale, the OST flux proxy generally followed the same seasonal magnitude and depth patterns as PC flux (Fig. 5). The two Navis floats were allowed to profile for approximately 5.5 days after recovery of the NBSTs in August 2013 in order to examine flux variability over a longer deployment period and intercompare the platforms (Table 2). While there was scatter in the 4–16 h OST proxy averages collected from the floats during this period, they generally clustered around the longer 2.5-d averages from the transmissometers on the NBSTs (Fig. 6). In order to compare attenuation flux magnitudes between the platform types in spite of mismatches in measurement depths, power-law functions ($F(z) = F(z_{ref})(z/z_{ref})^{-b}$) were fit to the NBST and Navis datasets. Extrapolating to $z_{ref} = 130 \text{ m}$, the attenuation flux $F(z_{ref})$ from the NBST was $0.0071 (\pm 0.0008) \text{ m}^2 \text{m}^{-2} \text{d}^{-1}$. From the Navis floats, $F(z_{ref})$ fit only to points shallower than 300 m (to match NBST depths) was $0.008 (\pm 0.002)$. $F(z_{ref})$ was $0.0078 (\pm 0.0006) \text{ m}^2 \text{m}^{-2} \text{d}^{-1}$ when measurements at 500 m were included. Unaveraged attenuation vs. time plots (similar to Fig. 2) for all individual NBST and Navis float deployments are shown in the Supplementary Information (Figs. S1–S3). The deployments reported in this study were too short to observe appreciable drift in absolute beam attenuation, as has been observed during longer deployments (Bishop et al., 2002; Estapa et al., 2013).

The signal derived from positive, discontinuous “jumps” in attenuation, normalized to deployment length, ranged from 0 to 0.0029 $\text{m}^2 \text{m}^{-2} \text{d}^{-1}$. Positive jumps occur in response to collection of rarer, large particles. Negative jumps, on the other hand, cannot result from passive flux and are not counted. Positive jumps were observed in 9 of 15 NBST deployments. This discontinuous signal was equivalent to 12–28% of the slowly-accumulating, continuous OST proxy signal in all

but two records. These two records, from the shallower March 2014 NBST deployments, had jump-derived signals that were 60% and 82% of the simultaneous, continuous OST proxy signals. These jump-derived signals exclude discontinuities that encompassed spikes, or occurred while the NBST was outside of the target depth range.

We assumed variability in the attenuation flux measured by the OST was due to three primary sources: 1) real, spatiotemporal variability in particle flux; 2) sensor noise; and 3) random variations in the detection rate of particles by the OST. We estimated the uncertainty in the OST flux proxy from this third source of variability, because propagated sensor noise was quite small (on average, $7.5 \times 10^{-4} \text{ m}^2 \text{m}^{-2} \text{d}^{-1}$). Gel trap-based estimates of particle number flux as a function of size (following a power-law model; Table 1; Durkin et al., 2015) were used to determine the average particle flux in logarithmically-spaced size bins across the cross-sectional area of the transmissometer beam during each deployment. Particle detection was assumed to follow a Poisson distribution, so that the uncertainty in the detection rate in each size class was equal to the square root of that class's mean particle detection rate. We converted the detection rate uncertainty to an attenuation flux uncertainty by multiplying by a particle attenuation efficiency of 2, assuming that all particles were large relative to the wavelength of light (Bohren and Huffman, 2004). For transparent particles, this may be an overestimate so the computed attenuation flux uncertainty may be conservatively large. Finally, we summed the uncertainties quadratically over all particle size classes. For comparison, the relative uncertainty in the attenuation flux estimated in this manner ranged from 6% to 31% of the deployment mean flux (Fig. 7), and as might be expected, was higher when fluxes were lower and when flux size distribution slopes were flatter (Table 1).

Same-platform (NBST) PC and deployment-averaged OST proxy measurements were positively correlated ($R^2 = 0.62$, $n = 15$). We performed a weighted, Type-II regression of ATN flux ($\text{m}^2 \text{m}^{-2} \text{d}^{-1}$) vs. PC flux ($\text{mg-C m}^{-2} \text{d}^{-1}$), with the inverse of individual samples' measurement uncertainties in both parameters used to weight points in the least-squares minimization (Fig. 7; Type II linear regression). We computed the carbon-to-attenuation flux ratio (PC:ATN) of settling particles at the BATS site as the inverse of this regression slope, giving a value of $3.8 (\pm 0.5) \times 10^3 \text{ mg-C m}^{-2}$ (uncertainty is the 95% confidence interval; Table 3). The March 2014 points clustered below the linear trendline, although removal of those points did not strongly affect the goodness-of-fit or regression line slope. Adding the cumulative, positive jump signal from each deployment to the OST proxy decreased the PC:ATN ratio to $3.4 (\pm 0.2) \times 10^3$ (Table 3) and improved the correlation with PC flux data ($R^2 = 0.66$), primarily through better correspondence of the OST proxy to PC flux in the two shallowest March 2014 observations (Fig. 7). In both cases (with and without the “jump” signal), the regression of ATN flux vs. PC flux had a non-zero y-intercept (positive attenuation flux at zero PC flux). The magnitude of this offset was $1 (\pm 0.4) \times 10^{-3} \text{ m}^2 \text{m}^{-2} \text{d}^{-1}$ with jumps included and $9 (\pm 4) \times 10^{-4} \text{ m}^2 \text{m}^{-2} \text{d}^{-1}$ without (Fig. 7). For this reason, we also performed a linear regression forced through a zero intercept (Fig. 7), which gave a PC:ATN ratio of $2.38 (\pm 0.08) \times 10^3 \text{ mg-C m}^{-2}$ with the jump signal included (Table 3). The projected particle cross-sectional area measured in the gels (data not shown) did not correspond well to the OST flux proxy or to trap fluxes, probably because the projected cross-sectional area in the gels was determined by adding up the areas inside the detected particle perimeters, without incorporating information on particle transparency (e.g., Figs. 2 and 7 in Durkin et al. (2015)). This is consistent with the discussion of Bishop (1999) that beam attenuation is a good proxy for POC because the non-organic (i.e., fluid) parts of particles do not contribute much to the total attenuation cross section.

Time and area-normalized counts of identifiable zooplankton in the gel trap collectors on the NBSTs decreased with depth (Fig. 8). The count rate of spikes, filtered out of the drift-phase ATN vs. time data prior to OST proxy computation, showed a similar pattern. When spike rates were normalized to the transmissometer beam cross-section, the

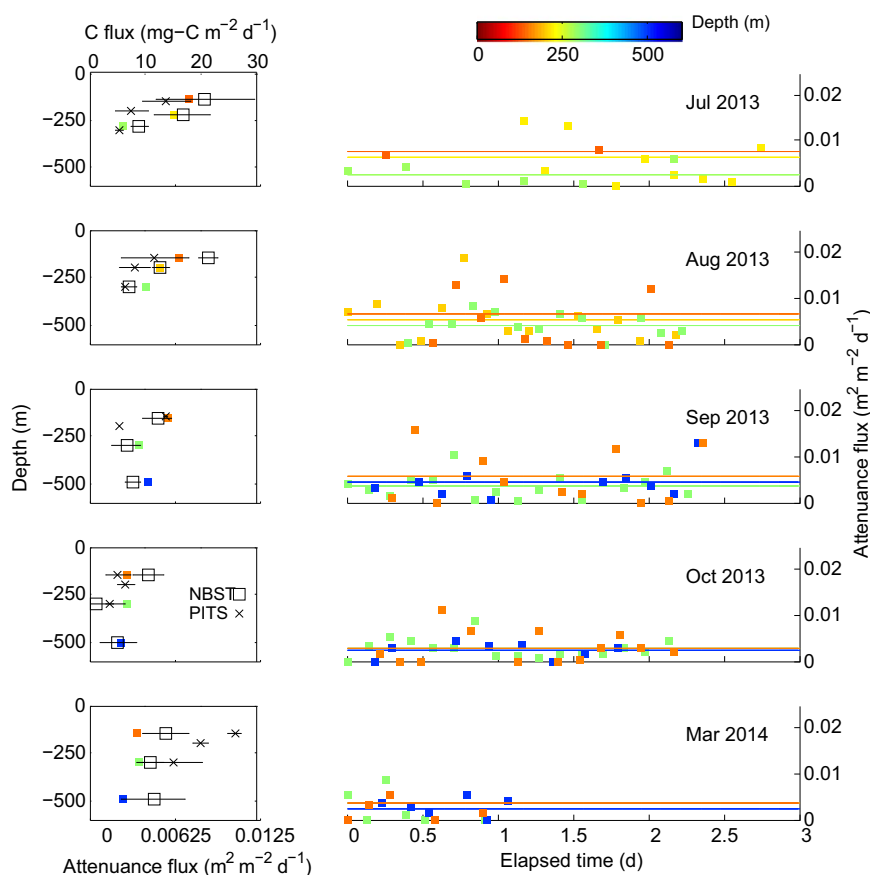


Fig. 5. Summary of carbon flux and attenuation flux measurements from transmissometers on the NBSTs. Left column of panels shows time-averaged carbon flux measurements from NBSTs (open squares), PITs (crosses), and OST attenuation flux measurements (colored squares) as a function of depth. Right column of panels shows the attenuation flux averaged over 3-h periods as a function of time during the deployment, with horizontal lines showing the average at each depth. Colors correspond to the left-hand panel colors and indicate NBST depth. Fairly good agreement was observed between the full attenuation flux averages and the measured carbon flux to the trap tubes. The OST flux proxy showed more time variability at 150 m as compared to deeper measurements. (For interpretation of the references to color in this figure legend, the reader is referred to the web version of this article.)

rate was 8 times higher than the zooplankton count rate. The two parameters were positively related ($R^2=0.64$, $n=14$, Fig. 8). We did not observe a similar relationship between jumps in the $c(650)$ vs. time data and zooplankton counts (data not shown).

3.2. Results of laboratory tests

Laboratory characterization of multiple scattering due to the settling of polystyrene beads on the transmissometer window indicated minimal effect of particle loading, up to beam attenuation values of almost 1 m^{-1} and for bead diameters ranging 25–250 μm (Fig. 9). Some noise was observed around the 1:1 line (RMSE=0.0582). Mass-specific attenuation coefficients of settled, monodisperse beads agreed well with theoretical predictions (van de Hulst, 1957; data not shown).

T. weissflogii cells had the lowest PC:ATN ratio of all particle assemblages measured in the laboratory, $3.0 \times 10^2 \text{ mg-C m}^{-2}$. Iselin pier surface plankton had a ratio of $6.5 \times 10^2 \text{ mg-C m}^{-2}$, and Saratoga Lake plankton had a ratio of $10.5 \times 10^2 \text{ mg-C m}^{-2}$ (Table 3). The Iselin pier sample contained primarily unidentifiable detritus, while the Saratoga Lake sample contained, in addition to detritus, *Asterionella* and *Fragilaria* diatoms, aggregates of green algae, and dead freshwater zooplankton.

4. Discussion

4.1. OST flux proxy calibration and interpretation

In this study we measured particulate carbon flux from three

different platforms (surface-tethered traps, NBSTs, and profiling floats) by two contrasting methods. Our goal was to calibrate the OST technique against direct PC flux measurements obtained via sediment traps. Because PC flux is highly spatially and temporally variable (Estapa et al., 2015), our empirical, field-based calibration of an OST vs. direct sediment trap measurements was based on observations that were minimally separated in space and in time. Transmissometer and trap observations made from the same NBST platforms showed a good correlation between the averaged OST proxy and the measured carbon flux. The OST calibration slope (Fig. 7) can be interpreted as a combination of 1) the intrinsic optical properties of the sinking particles (i.e., the PC:ATN ratio described above); 2) the particle-collection efficiency of the transmissometer on its host platform; and 3) the detection efficiency of the transmissometer for particles accumulated on the sensor's optical window. The positive y-intercept in the OST calibration (Fig. 7), and the associated difference in the slopes of the two tested regression models, similarly could stem simultaneously from a number of causes— undercollection by the NBSTs at low fluxes, solubilization of trap samples prior to recovery, removal of a small amount of passively-settled flux along with swimmers from NBST samples, undercollection of fast-sinking particles by the transmissometer (Estapa et al., 2013), or an increasing PC:ATN ratio at higher PC fluxes. As the y-intercept magnitude is comparable to the variability in the PC flux measurements, we cannot yet attribute it with confidence to any of these possible causes. Further, the former, trapping-related sources of uncertainty are difficult to constrain and have been discussed in detail elsewhere (Buesseler et al., 2007; Owens et al., 2013). We note that Bishop et al. (2016) have also reported ATN fluxes

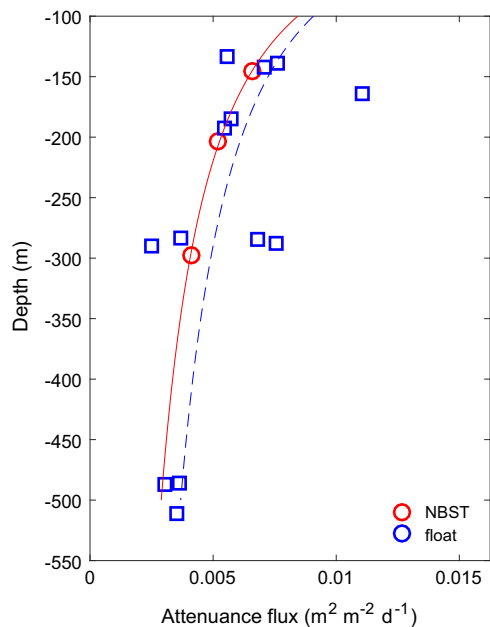


Fig. 6. OST proxy measurements from transmissometers on the NBSTs (red circles) in August 2013, and on two profiling floats deployed for a period of 8 days during and following the NBST deployment (blue squares). Also see Tables 1, 2 for deployment summaries. Each NBST deployment averaged over approximately 2.5 days, while each float drift phase ranged from 4 to 16 h long. Red line shows a power-law fit through the NBST points while blue dashed line shows a power-law fit through the float points. The best-fit parameter values and 95% confidence intervals of the power-law fits are: $F(z) = 0.0071 \pm 0.0008 (z/130)^{-0.67 \pm 0.25}$ (for NBSTs); and $F(z) = 0.0078 \pm 0.0006 (z/130)^{-0.56 \pm 0.12}$ (Navis floats), where $F(z)$ is attenuation flux ($\text{m}^2 \text{m}^{-2} \text{d}^{-1}$) at depth z . (For interpretation of the references to color in this figure legend, the reader is referred to the web version of this article.)

derived from an imaging sensor deployed in the California coastal current, and during low export periods their measurements, ranging from 0.002 to 0.007 $\text{m}^2 \text{m}^{-2} \text{d}^{-1}$, were similar to those we report here for the BATS site (Figs. 5–7). Here we focus our discussion primarily on the carbon-to-optical surface area ratios of sinking particles, and the particle-collection and particle-detection efficiencies of a transmissometer used as an optical sediment trap.

In situ measurements prevent the easy separation of different factors contributing to the OST calibration slope, so we used laboratory tests to measure the detection efficiency of the transmissometer and the optical properties of sinking-particle analogs. We did not find evidence of multiple scattering (e.g., Kiefer and Soohoo, 1982) for particles settled on the transmissometer's optical window rather than distributed throughout the sampling volume, even for attenuation fluxes much larger than would be measured in the field (Fig. 9); and compare to data in Estapa et al. (2013). A typical beam attenuation measurement averages over many realizations of the suspended particles' changing spatial distribution in a mixing fluid. The OST technique measures attenuation of settled particles, which introduces a new source of uncertainty due to the fact that particles are not moving, so that each measurement captures only a single realization of the spatial distribution of particles with respect to optical sampling volume. In low-flux environments like the BATS site, the largest particles are also rare and their low numbers contribute noise to the relationship. These sources of uncertainty are present in Fig. 9 and likely contribute to the variability in Fig. 7.

4.2. Carbon-to-attenuance flux ratios in sinking particles

The literature contains many field measurements of the ratio of particulate carbon concentration to beam attenuation in suspended particles, which is analogous to the PC:ATN flux ratio reported here for

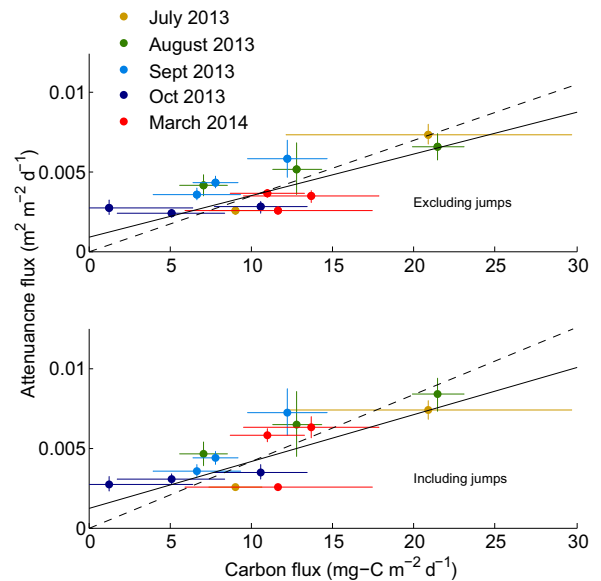


Fig. 7. Calibration curve for OST flux proxy based on field data from NBSTs. Different colors represent different cruises, and horizontal error bars are standard deviations among triplicate trap tubes (or ranges among duplicates). Vertical error bars show the estimated uncertainty of attenuation flux derived from the gel trap particle size distribution (see text). Solid lines show weighted Type-II fits; dashed lines show regression forced through zero. Top panel: OST proxy from attenuation rate of change excluding “jumps” ($R^2 = 0.62$). Regression without “jump” signal, weighted Type-II fit parameters ($\pm 95\%$ confidence intervals): $y = 2.6 (\pm 0.3) * 10^{-4} * x + 9.0 (\pm 0.4) * 10^{-4}$. Regression without “jump” signal forced through zero: $y = 3.5 (\pm 0.1) * 10^{-4} * x$. Bottom panel: OST proxy with addition of time-normalized “jump” signal ($R^2 = 0.66$). Regression line including “jump” signal, weighted Type-II fit: $y = 3.0 (\pm 0.4) * 10^{-4} * x + 1 (\pm 0.4) * 10^{-3}$. Regression including “jump” signal forced through zero: $y = 4.2 (\pm 0.1) * 10^{-4} * x$. (For interpretation of the references to color in this figure legend, the reader is referred to the web version of this article.)

sinking particles (both ratios bear units of mg-C m^{-2}). Carbon:attenuation ratios for suspended particles range from approximately 300 to 600 mg-C m^{-2} (e.g., Marra et al., 1995, Gardner et al., 2006, Bishop and Wood, 2008, Cetinić et al., 2012). One estimate of PC:ATN for sinking particles is given by Bishop et al. (2016); this is equivalent to 33,200 mg-C m^{-2} but is based upon assumed, rather than directly-measured, carbon content of the particles. Measurements of fecal pellets (e.g., Dagg et al., 2014 and references therein; diameter ranges of 0:10–1000 μm) and phytoplankton cells (Menden-Deuer and Lessard, 2000; diameter ranges of 0:1–100 μm) show carbon contents increasing approximately linearly as a function of volume (i.e., carbon per area increases as a function of diameter). This suggests that larger sinking particles should have more carbon per attenuation than suspended particles due to their larger volume-to-surface area ratios. However, observations of marine snow aggregates ranging in diameter from order 1–10 mm show decreasing carbon per surface area as particle size increases, presumably due to the fractal nature of the aggregates (Alldredge, 1998). Yet other studies have found the mass-specific beam attenuation of marine aggregates to be similar to that of the disaggregated primary particles making up the aggregates, suggesting that carbon per attenuation should be approximately constant as a function of particle size (Boss et al., 2009b; Slade et al., 2011).

In order to better compare our own measurements of PC:ATN to carbon:volume estimates from the literature, we used the models of Menden-Deuer and Lessard (2000; diatoms, dinoflagellates, and non-diatom protists), Dagg et al. (2014; fecal pellets), and Alldredge (1998; diatom and fecal marine snow) to predict carbon contents of particles ranging in size from 10 to 1000 μm . We then computed theoretical attenuation cross-sections for equivalently-sized spheres (attenuance cross-section is twice the geometric cross section for particles large relative to the wavelength of light; Bohren and Huffman, 2004).

Table 3
Settling-particle optical properties.

Field or lab sample	Carbon: attenuation flux ratio (\pm 95% confidence) (mg C m^{-2})
BATS, type-II weighted regression	$3.4 \pm 0.2 \times 10^3$
BATS, type-II weighted regression excluding “jump” signal (see text)	$3.8 \pm 0.5 \times 10^3$
BATS, regression forced through zero	$2.38 \pm 0.08 \times 10^3$
<i>T. weissflogii</i> culture	$3.0 \pm 0.3 \times 10^2$
Iselin pier, Woods Hole, MA	$6.5 \pm 0.8 \times 10^2$
Saratoga Lake, Saratoga Springs, NY	$1.1 \pm 0.1 \times 10^3$

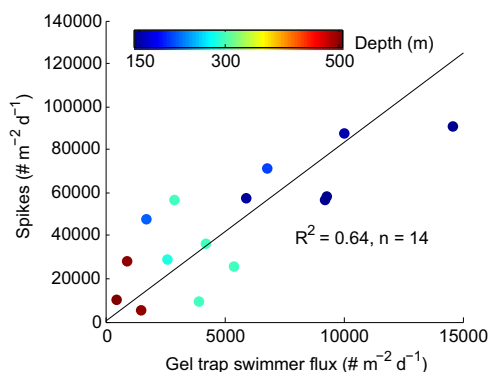


Fig. 8. Rate of occurrence of spikes in the OST flux proxy vs. gel trap zooplankton “swimmer” flux (normalized to optical beam cross-sectional area, or gel area counted, and to deployment length). The good correlation between the two suggests that spikes in the flux proxy signal are related to the presence of active swimmers around the trap. (For interpretation of the references to color in this figure legend, the reader is referred to the web version of this article.)

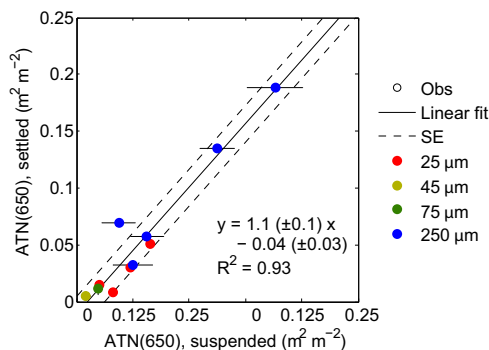


Fig. 9. Attenuance measured for suspended polystyrene beads of various sizes and concentrations (x-axis) and the same suspensions' attenuation values after allowing beads to settle. Horizontal error bars are the 15th–85th percentile range of approximately 1 min of observations (at 1 Hz) while suspensions were allowed to flow through the transmissometer. Parameters for Type-II linear regression are given. We did not see evidence of multiple scattering due to particle settling. Noise in the relationship may be due, in part, to the fact that settled particles do not move around in the beam cross-section, while suspended particles do. (For interpretation of the references to color in this figure legend, the reader is referred to the web version of this article.)

Finally, we computed the theoretical PC:ATN ratio for each particle type. These estimates are shown as a function of size in Fig. 10 (solid lines). Fig. 10 also shows the bulk (i.e., not-size resolved) estimates of PC:ATN based on measured (rather than assumed) attenuances from this study and from Bishop et al. (2016) using dashed, horizontal lines. Our estimated PC:ATN for BATS is most consistent with the smaller size classes of fecal marine snow estimated from Alldredge (1998), and with the fecal pellet estimate based on the model of Dagg et al. (2014). These particle types are primarily what Durkin et al. (2015) identified in the gel collectors during the BATS deployments.

Our field measurements of sinking particles at the BATS site (Fig. 7) gave a PC:ATN ratio that was larger than the largest values reported for suspended particles (see Fig. 10 for values derived from the Menden-

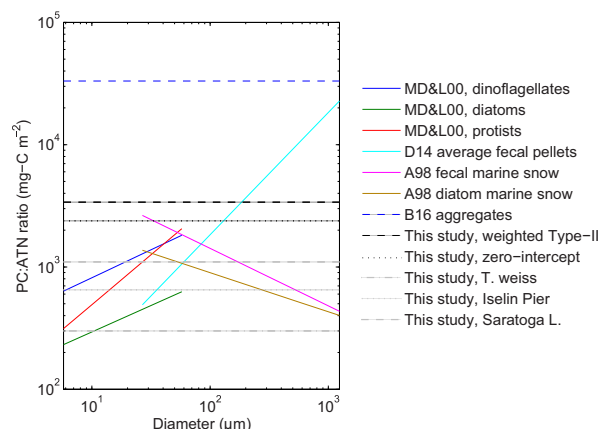


Fig. 10. Values of PC:ATN ratios derived from literature models of particle carbon content as a function of size, for different particles types relevant to sinking flux (see text for discussion). Also included are bulk PC:ATN ratios from this study and from Bishop et al. (2016). Solid lines show model-derived PC:ATN values as a function of particle size. “MD & L00” refers to models of dinoflagellates, diatoms, and non-diatom protists from Menden-Deur and Lessard (2000). “D14” refers to average literature values for fecal pellets from Dagg et al. (2014). “A98” refers to values for fecal and diatom-derived marine snow from Alldredge (1998). Horizontal, dashed lines show bulk (not particle-size specific) PC:ATN ratios computed from measured attenuances. “B16” refers to the calibration ratio for California Current sinking particles derived by Bishop et al. (2016). Black and gray dashed lines show the various PC:ATN ratios from this study (Table 3). (For interpretation of the references to color in this figure legend, the reader is referred to the web version of this article.)

Deur and Lessard (2000) estimates for plankton cells; and Table 1 in Cetinić et al. (2012)). Sinking-particle assemblages from Iselin Pier and Saratoga Lake also had PC:ATN values at the high end of values observed for suspended particles (Table 3; Fig. 10), although not as high as at the BATS site. This could reflect aggregates with lower fractal dimension or compositional differences compared to the BATS site, but because our model assemblages were from shallow water in inland and near-coastal environments, their lower PC:ATN ratios may also reflect higher lithogenic contributions, or collection differences between the laboratory and field measurements. The settled *T. weissflogii* cells measured here in the lab had PC:ATN ratios (Table 3) similar to field measurements of non-sinking diatom communities referenced above. This is consistent with findings that aggregates have similar carbon: surface area properties to their primary particles.

We did not find a significant relationship between individual field samples' PC:ATN ratios and their particle size distributions determined from gel trap images (Table 1; Durkin et al., 2015). Also, the OST flux proxy was a much better predictor of carbon flux over all 5 cruises ($R^2 = 0.66$) compared to the total particle area flux in the gels ($R^2 = 0.02$; Durkin et al., 2015). This could be due to particles having sizes that are large relative to the wavelength of visible light, but optical properties that are better modeled as a collection of small particles in the Mie scattering regime with some variable, non-attenuating fluid fraction (Boss et al., 2009b; Slade et al., 2011). Durkin et al. (2015) modeled the carbon content of particles (C) in our samples from BATS as a power-law function of particle diameter ($C(D) = \alpha(D)^\beta$) for each cruise month using the bulk PC fluxes and gel trap PSD data, and found that values of

β fell between 2 and 3. This implies that larger particles had increasing carbon content relative to surface area (i.e., $\beta=2$ corresponds to carbon increasing linearly with surface area which scales with D^2). The PC:ATN ratio may also depend on the particle fractal dimension (Jackson et al., 1997), with solid, spherical particles (high fractal dimension) having greater PC:ATN ratios than fluffy, non-spherical particles (low fractal dimension) with the same overall diameter. The existence of a non-zero offset in the linear regression fit to the OST calibration data set (Fig. 7) is consistent with the presence of larger particles at higher fluxes and implies that a nonlinear calibration might be appropriate to test, pending collection of additional calibration data at higher fluxes.

The full range of settling-particle optical properties remains to be characterized in future studies. Both the PC:ATN ratios of settled *T. weissflogii* aggregates (Table 3) and the mass:ATN ratios of settled polystyrene beads of various sizes (not shown), were respectively consistent with field measurements (Cetinić et al., 2012) and theoretical predictions (van de Hulst, 1957) for those particle types in suspension. This result shows that particles should have the same PC:ATN properties whether they are measured in suspension or settled in a layer. However, just as for suspended particles, instrument acceptance-angle effects (Voss and Austin, 1993; Bishop and Wood, 2008; Boss et al., 2009a) may decrease the sensitivity of the OST measurement to larger particles, and comparisons between measurements made with transmissometers with difference acceptance angles require care in interpretation. Like any optical proxy for ocean biogeochemical parameters, sensor calibration against direct measurements in the region of interest is critical for correct interpretation of the proxy data.

4.3. Platform considerations

One potential source of uncertainty in the OST proxy measurements of PC flux is the possibility of uncorrected vertical shading of the upward-looking transmissometer face by the top part of the transmissometer housing, and for the NBST, the upper trap tube support plate. Estapa et al. (2013) used a conservative estimate of the turbulence dissipation rate ($\epsilon=10^{-9.5} \text{ m}^2 \text{ s}^{-3}$) in the ocean interior, at a depth of 1000 m where the floats in that study sampled, to estimate the horizontal turbulent velocity that would be experienced by settling particles. Note that motions at scales larger than the float platform were not included in the estimate as the float is quasi-Lagrangian at those scales (Lien et al., 1998; D'Asaro, 2003). At $\epsilon=10^{-9.5} \text{ m}^2 \text{ s}^{-3}$, modeled particles settling faster than 130 m d^{-1} would begin to feel the effects of vertical shading (Estapa et al., 2013) by the upper part of the transmissometer housing, and hence also require correction for horizontal shielding. This velocity is almost an order of magnitude faster than average particle settling velocities at the BATS site (McDonnell and Buesseler, 2012). Furthermore, a recent compilation of global, depth-resolved measurements of turbulence in the ocean interior (Waterhouse et al., 2014) shows that ϵ ranges from 10^{-10} to $10^{-8} \text{ m}^2 \text{ s}^{-3}$ in the upper 1000 m through most of the global ocean, with higher values likely near boundaries (coasts and topographic features) and in areas of internal wave generation (shallower in the thermocline). As the data presented here were all collected at depths of 500 m and shallower, it is unlikely that vertical shading impacted Navis-based OST measurements reported here. While the simple turbulence estimate of Estapa et al. (2013) does not apply to the shading geometry of the NBST-based OST, we observed that attenuation fluxes to co-deployed Navis floats and NBSTs (Fig. 6) were in better agreement than the 20% variability among co-deployed NBSTs typically observed in similar studies (Lamborg et al., 2008; Owens et al., 2013). This supports the possibility that in this study, the NBST-OSTs were not strongly impacted by shading.

Application of the OST proxy in other settings should consider the platform-specific dependence of horizontal shielding on vertical shad-

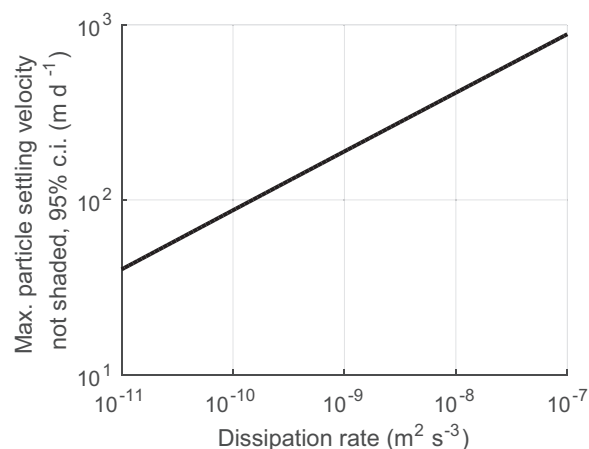


Fig. 11. The modeled, threshold (95% c.i.) sinking velocity above which vertical shading and horizontal shielding are predicted to impact OST measurements using a 25 cm pathlength transmissometer, plotted as a function of dissipation rate ϵ . The x-axis range encompasses most oceanic dissipation rate conditions, from the deep ocean away from boundaries, to the upper ocean. The unshaded particle sinking velocities estimated here are based on a completely unshaded OST (open on all sides) and should be interpreted carefully when an OST is deployed in a setting with rapidly-sinking particles on a platform that causes appreciable shading.

ing, as well as the combined impacts of particle settling velocity and ambient turbulence. We extended the simple estimate of Estapa et al. (2013) across a range of possible particle settling velocities ($10\text{--}4000 \text{ m d}^{-1}$) and dissipation rates ($\epsilon=10^{-11}\text{--}10^{-7} \text{ m}^2 \text{ s}^{-3}$) and computed the threshold particle settling velocities above which vertical shading is likely (95% confidence interval) when observations are made with transmissometer with dimensions identical to the C-Rover 2K, carried aboard a profiling float similar to the Navis BGCi. Fig. 11 plots the threshold sinking velocity as a function of dissipation rate. At $\epsilon=10^{-10} \text{ m}^2 \text{ s}^{-3}$, particles settling at just under 100 m d^{-1} will start to be undercollected, with the degree of undercollection increasing with settling speed. At $\epsilon=10^{-9} \text{ m}^2 \text{ s}^{-3}$, shading will not set in until particle settling speeds exceed about 200 m d^{-1} , and at $\epsilon=10^{-8} \text{ m}^2 \text{ s}^{-3}$, only particles settling faster than 423 m d^{-1} are likely to be undercollected. These estimates are idealized and do not consider possible anisotropy or “wake effects” around the small-scale structures of the OST and host platforms.

Another effect of ambient, relative fluid motion around the drifting OST could be to wash accumulated particles off of the upward-facing transmissometer window. Observations of Estapa et al. (2013) showed that the first 100–500 m of profile ascent (at a nominal speed of $8\text{--}10 \text{ cm s}^{-1}$) after the termination of a 2-d drift phase typically led to window clearance. However, factors such as ballasting inaccuracies, buoyancy adjustments by the platform, incompletely-attenuated surface gravity waves and internal waves cause small vertical motions of the platform during the drift phase (Figs. S1–S3). In the deployments conducted here, these motions did not show any systematic correspondence to jumps or spikes, although occasionally vertical motions into and out of the particle maximum led to variations in the attenuation vs. time record (e.g., Fig. S1, 150 m, July 2013), which reduced the fraction of the record that could be used to estimate the particle flux. The amount of vertical motion necessary to dislodge accumulated particles may be a function of particle stickiness or related to the extent of window fouling over the length of the deployment. For instance, Estapa et al. (2013) found that absolute, deep-water beam attenuation values sometimes, but not always, increased slowly over many profile cycles during long-term deployments (rates ranged from -8×10^{-5} – $1.7\times 10^{-2} \text{ m}^{-1} \text{ d}^{-1}$). Exact causes of this drift, which affects beam attenuation profiles but not the OST attenuation flux measurements described here, remain to be determined in future work but appear to be most related to biological productivity of the deployment area

(Estapa et al., 2013).

Differences between PC fluxes measured by NBSTs and PITs (Fig. 5) were consistent with a previous, intensive three-year inter-comparison (Owens et al., 2013), and possibly caused by differences in platform hydrodynamics and sampling procedures. The high-spatial resolution PC flux models and measurements of which we are aware (Fig. 5; Buesseler et al., 2009; Resplandy et al., 2012; Jackson et al., 2015; Estapa et al., 2015) also show that export is very patchy at scales of a few kilometers, which could also lead to the observed differences between NBSTs and PITs, and to the large variability observed in the OST signal at short time resolutions as compared to averages over entire deployments (Fig. 6). This spatial and temporal variability in particle flux is also reflected in the averaged OST proxy observations from three NBSTs and two profiling floats in August 2013 (Fig. 6). Causes of such patchiness could be due to biological factors, or to the presence of eddies or submesoscale fronts around eddies (Guidi et al., 2007; Estapa et al., 2015). The variability in the OST signal is also consistent with the infrequent collection of rare, large particles, for which the BATS site represents a worst-case scenario where low fluxes are dominated by relatively small particles (Table 1; Durkin et al., 2015). In such cases, averaging the OST flux proxy over long periods and carefully intercalibrating it with larger collection-area traps, such as we have done here, or a different proxy such as the ^{234}Th deficit, would be important.

Our OST measurements detected “spike” signals consistent with the presence of the same zooplankton “swimmers” that are known to actively enter traditional sediment traps (Lee et al., 1988). The area-normalized swimmer flux in the gel traps was positively related to the transmissometer signal spike rate (Fig. 8). The higher area-normalized spike “flux” (about 8 times the swimmer flux) could reflect 1) physical and behavioral differences in how zooplankton interact with brine-filled traps vs. with an optical sensor, and 2) multiple passages of the same individual in and out of the beam. We found no relationship between the number of discontinuous jumps in the transmissometer signal and spikes, or between jumps and swimmer fluxes. The improvement in the fit of the OST proxy to the measured PC flux when a subset of positive jumps were included as part of the flux signal suggests that at least some of the time, such jumps were related to large particles passively settling onto the optical window between consecutive 15 min observations. This subset excluded negative jumps and positive jumps coinciding with spikes and wrong-depth points. The number and size of these jumps was not related to the particle size distribution slope measured in the gel traps (Table 1). Gentle physical interference with the instrument during laboratory measurements of settled particle properties also caused jumps in the c_p vs. time signal, anecdotally suggesting that local turbulence, platform motion, or slumping of material on or off of the optical window may also have been responsible for some of those features.

4.4. Suggestions for future OST application and development

We have presented an initial, empirical calibration of the OST proxy for particulate carbon flux. The behavior of the instrument is consistent with our understanding of particle optics and points toward future, more widespread use of this proxy to make broader carbon flux measurements in undersampled areas of the ocean. Further method refinements should include expanded laboratory and field measurements of settling particles’ sizes, settling velocities, and compositions (i.e. fractions of organics, opal, and carbonate), both to ensure good calibration of the optical proxy for each deployment, and to separate issues of transmissometer collection efficiency and acceptance-angle effects from variability in settling-particle optical properties, which are still poorly constrained. Better understanding of the controls on specifically *sinking* particles’ optical properties is important for all autonomous, optical methods of measuring settling PC flux, not just the OST method. Uncertainties due to complex platform hydrodynamics

are currently based on the idealized estimates presented here, which could be improved upon with collection of *in situ* measurements and detailed numerical modeling of flow around platforms. Unaccounted shading of the sensor from sinking particles is the most likely bias and would mean that our estimates of PC:ATN ratios are high. OSTs simultaneously deployed on Navis floats and NBSTs agree with one another (Fig. 6) in spite of differing platform geometries, for instance the upper trap support plate on the NBST (Fig. 1). However, we cannot unequivocally rule out shading. Because sinking particles at BATS may have had slow settling velocities (McDonnell and Buesseler, 2012), future use of the OST with platforms such as the NBST in other settings should include tests assessing whether there is a bias against collection of more rapidly-settling particles. Future work ought to also focus on field intercomparisons of different methods for measuring PC flux, which all have their advantages and disadvantages.

Implementation of the OST method as part of a distributed, autonomous sampling network (e.g., Bio-Argo) would require the inclusion of a transmissometer or other simple attenuation sensor and a tilt sensor as part of the float’s bio-optical sensor package, as well as collection of sensor data every 15 min during the “park” phase of the float’s mission cycle. At a minimum, data from the transmissometer, tilt and pressure sensors must be collected during the drift phase, although accompanying scattering, conductivity, and temperature data can also provide useful information for OST flux interpretation and should be collected if technically feasible. The profile cycle length (time between successive resurfacings) was set in this study to 1.5–3 days to minimize degradation of sediment trap samples prior to collection. In an autonomous implementation, the cycle length should be short enough to resolve variations in water column bio-optical properties, but long enough to resolve the flux processes of interest. To avoid uncertainties in the interpretation of attenuation flux data, drift depths should be selected so that small vertical motions of the drifting platform do not cross in and out of the surface particle maximum layer. The transmissometer can be used to measure both attenuation flux and beam attenuation. Attenuance flux, as discussed here, is a relative measurement not impacted by long-term sensor drift (Estapa et al., 2013), but when the float is deployed under productive conditions, beam attenuation may require a correction such as subtraction of a deep-water offset, regardless of whether the window is subjected to a rinsing operation (Bishop et al., 2002, 2004; Bishop and Wood, 2009; Estapa et al., 2013).

The observations presented here show that spatiotemporal variability in particulate carbon export at small scales is important, even though it is not typically observed in direct sediment trap samples or using other autonomous sensor-based proxies, because of their time-integrating natures. Intercalibrations of one PC flux measurement method against another must account for this variability, preferably by making observations from the same platform, or alternatively by averaging across larger spatiotemporal scales. Finally, it is important to characterize variability in export flux because it may contain information about small-scale processes comprising the biological pump.

Acknowledgements

Funding for this project was provided by the NSF Chemical Oceanography program (OCE-1260001/1406552). MLE and CD have been supported by WHOI Postdoctoral Scholar Fellowships. We are grateful to the BATS team at BIOS for providing field assistance and shore-based facilities and to the captain and crew of the *R/V Atlantic Explorer*. Dennis McGillicuddy and Valery Kosnyrev (WHOI) provided SLA analyses, with support from NASA and NSF. SLA data were distributed by Collecte Localis Satellites, AVISO (<http://www.avisooceanobs.com>). Sea-Bird Electronics and WETLabs provided float and sensor operational support and advice. This manuscript was greatly improved by the detailed and insightful comments of Nathan Briggs and three anonymous reviewers. Data are available upon request from

the authors.

Appendix A. Supplementary material

Supplementary data associated with this article can be found in the online version at doi:10.1016/j.dsr.2016.12.003.

References

- Allredge, A., 1998. The carbon, nitrogen and mass content of marine snow as a function of aggregate size. *Deep Sea Res. Part I: Oceanogr. Res. Pap.* 45, 529–541.
- Alonso-Gonzalez, L.J., Aristegui, J., Lee, C., Sanchez-Vidal, A., Calafat, A., Fabres, J., Sangra, P., Masque, P., Hernandez-Guerra, A., Benitez-Barrios, V., 2010. Role of slowly settling particles in the ocean carbon cycle. *Geophys. Res. Lett.* 37, L13608.
- Bishop, J.K.B., 1999. Transmissometer measurement of POC. *Deep Sea Res. Part I: Oceanogr. Res. Pap.* 46, 353–369. [http://dx.doi.org/10.1016/S0967-0637\(98\)00069-7](http://dx.doi.org/10.1016/S0967-0637(98)00069-7).
- Bishop, J.K.B., 2009. Autonomous observations of the ocean biological carbon pump. *Oceanography* 22, 182–193.
- Bishop, J.K.B., Davis, R.E., Sherman, J.T., 2002. Robotic observations of dust storm enhancement of carbon biomass in the North. *Pac. Sci.* 298, 817–821.
- Bishop, J.K.B., Fong, M.B., Wood, T.J., 2016. Robotic observations of high wintertime carbon export in California coastal waters. *Biogeosciences Discuss.* 2016, 1–32. <http://dx.doi.org/10.5194/bg-2016-62>.
- Bishop, J.K.B., Wood, T.J., 2009. Year-round observations of carbon biomass and flux variability in the Southern Ocean. *Glob. Biogeochem. Cycles*, 23. <http://dx.doi.org/10.1029/2008GB003206>.
- Bishop, J.K.B., Wood, T.J., 2008. Particulate matter chemistry and dynamics in the twilight zone at VERTIGO ALOHA and K2 sites. *Deep Sea Res. Part I: Oceanogr. Res. Pap.* 55, 1684–1706. <http://dx.doi.org/10.1016/j.dsr.2008.07.012>.
- Bishop, J.K.B., Wood, T.J., Davis, R.A., Sherman, J.T., 2004. Robotic observations of enhanced carbon biomass and export at 55 S during SOFeX. *Science* 304, 417–420. <http://dx.doi.org/10.1126/science.1087717>.
- Bohren, C.F., Huffman, D.R., 2004. *Absorption and Scattering of Light by Small Particles*. Wiley-VCH.
- Boss, E., Slade, W.H., Behrenfeld, M., Dall'Olmo, G., 2009a. Acceptance angle effects on the beam attenuation in the ocean. *Opt. Express* 17, 1535–1550.
- Boss, E., Slade, W., Hill, P., 2009b. Effect of particulate aggregation in aquatic environments on the beam attenuation and its utility as a proxy for particulate mass. *Opt. Express* 17, 9408–9420.
- Briggs, N., Perry, M.J., Cetinic, I., Lee, C., D'Asaro, E., Gray, A.M., Rehm, E., 2011. High-resolution observations of aggregate flux during a sub-polar North Atlantic spring bloom. *Deep Sea Res. Part I: Oceanogr. Res. Pap.* 58, 1031–1039. <http://dx.doi.org/10.1016/j.dsr.2011.07.007>.
- Buesseler, K.O., Pike, S., Maiti, K., Lamborg, C.H., Siegel, D.A., Trull, T.W., 2009. Thorium-234 as a tracer of spatial, temporal and vertical variability in particle flux in the North Pacific. *Deep Sea Res. Part I: Oceanogr. Res. Pap.* 56, 1143–1167. <http://dx.doi.org/10.1016/j.dsr.2009.04.001>.
- Buesseler, K.O., Antia, A.N., Chen, M., Fowler, S.W., Gardner, W.D., Gustafsson, O., Harada, K., Michaels, A.F., Rutgers van der Loeff, M., Sarin, M., et al., 2007. An assessment of the use of sediment traps for estimating upper ocean particle fluxes. *J. Mar. Res.* 65, 345–416.
- Cetinic, I., Perry, M.J., Briggs, N.T., Kallin, E., D'Asaro, E.A., Lee, C.M., 2012. Particulate organic carbon and inherent optical properties during 2008 North Atlantic Bloom Experiment. *J. Geophys. Res.*, 117. <http://dx.doi.org/10.1029/2011JC007771>.
- Dagg, M.J., Jackson, G.A., Checkley, D.M., 2014. The distribution and vertical flux of fecal pellets from large zooplankton in Monterey bay and coastal California. *Deep Sea Res. Part I: Oceanogr. Res. Pap.* 94, 72–86. <http://dx.doi.org/10.1016/j.dsr.2014.09.001>.
- Dall'Olmo, G., Mork, K.A., 2014. Carbon export by small particles in the Norwegian Sea. *Geophys. Res. Lett.* 41, 2921–2927. <http://dx.doi.org/10.1002/2014GL059244>.
- D'Asaro, E.A., 2003. Performance of autonomous Lagrangian floats. *J. Atmos. Ocean. Technol.* 20, 896–911.
- Durkin, C.A., Estapa, M.L., Buesseler, K.O., 2015. Observations of carbon export by small sinking particles in the upper mesopelagic. *Mar. Chem.* 175, 72–81. <http://dx.doi.org/10.1016/j.marchem.2015.02.011>.
- Ebersbach, F., Trull, T., 2008. Sinking particle properties from polyacrylamide gels during the Kerguelen Ocean and Plateau compared Study (KEOPS): zooplankton control of carbon export in an area of persistent natural iron inputs in the Southern Ocean. *Limnol. Oceanogr.* 53, 212–224.
- Estapa, M.L., Buesseler, K., Boss, E., Gerbi, G., 2013. Autonomous, high-resolution observations of particle flux in the oligotrophic ocean. *Biogeosciences* 10, 5517–5531. <http://dx.doi.org/10.5194/bg-10-5517-2013>.
- Estapa, M.L., Siegel, D.A., Buesseler, K.O., Stanley, R.H.R., Lomas, M.W., Nelson, N.B., 2015. Decoupling of net community and export production on submesoscales in the Sargasso Sea. *Glob. Biogeochem. Cycles*. <http://dx.doi.org/10.1002/2014GB004913>, (2014GB004913).
- Gardner, W.D., Mishonov, A.V., Richardson, M.J., 2006. Global POC concentrations from in-situ and satellite data. *Deep Sea Res. Part II: Top. Stud. Oceanogr.* 53, 718–740. <http://dx.doi.org/10.1016/j.dsr2.2006.01.029>.
- Guidi, L., Stemmann, L., Legendre, L., Picherat, M., Prieur, L., Gorsky, G., 2007. Vertical distribution of aggregates (> 110 μm) and mesoscale activity in the northeastern Atlantic: Effects on the deep vertical export of surface carbon. *Limnol. Oceanogr.* 52, 7–18.
- Jackson, G.A., Maffione, R., Costello, D.K., Allredge, A.L., Logan, B.E., Dam, H.G., 1997. Particle size spectra between 1 μm and 1 cm at Monterey Bay determined using multiple instruments. *Deep Sea Res. Part I: Oceanogr. Res. Pap.* 44, 1739–1767.
- Jackson, G.A., Checkley, D.M., Jr., Dagg, M., 2015. Settling of particles in the upper 100 m of the ocean detected with autonomous profiling floats off California. *Deep Sea Res. Part I: Oceanogr. Res. Pap.* 99, 75–86. <http://dx.doi.org/10.1016/j.dsr.2015.02.001>.
- Kiefer, D.A., Soohoo, J.B., 1982. Spectral absorption by marine particles of coastal waters of Baja California. *Limnol. Oceanogr.* 27, 492–499.
- Knap, A.H., Michaels, A.F., Steinberg, D.K., Bahr, F., Bates, N.R., Bell, S., Countway, P., Close, A., Doyle, A., Howse, F., Gundersen, K., Johnson, R.J., Little, R., Orcutt, K., Parsons, R., Rathbun, C., Sanderson, M., Stone, S., 1997. *BATS Methods Manual*. U.S. JGOFS Planning Office, Woods Hole.
- Lamborg, C.H., Buesseler, K.O., Valdes, J., Bertrand, C.H., Bidigare, R., Manganini, S., Pike, S., Steinberg, D., Trull, T., Wilson, S., 2008. The flux of bio-and lithogenic material associated with sinking particles in the mesopelagic “twilight zone” of the northwest and north central Pacific Ocean. *Deep Sea Res. Part II: Top. Stud. Oceanogr.* 55, 1540–1563.
- Lee, C., Wakeham, S.G., Hedges, J.I., 1988. The measurement of oceanic particle flux – are “swimmers” a problem? *Oceanography* 11, 34–36.
- Levy, M., Bopp, L., Karleskind, P., Resplandy, L., Etche, C., Pinsard, F., 2013. Physical pathways for carbon transfers between the surface mixed layer and the ocean interior: physical carbon fluxes. *Glob. Biogeochem. Cycles* 27, 1001–1012. <http://dx.doi.org/10.1002/gbc.20092>.
- Lien, R.-C., D'Asaro, E.A., Dairiki, G.T., 1998. Lagrangian frequency spectra of vertical velocity and vorticity in high-Reynolds-number oceanic turbulence. *J. Fluid Mech.* 362, 177–198.
- Lomas, M.W., Bates, N.R., Johnson, R.J., Knap, A.H., Steinberg, D.K., Carlson, C.A., 2013. Two decades and counting: 24-years of sustained open ocean biogeochemical measurements in the Sargasso Sea. *Deep Sea Res. Part II: Top. Stud. Oceanogr.* 93, 16–32. <http://dx.doi.org/10.1016/j.dsr2.2013.01.008>.
- Marra, J., Langdon, C., Knudson, C.A., 1995. Primary production, water column changes, and the demise of a Phaeocystis bloom at the Marine Light-Mixed Layers site (59°N, 21°W) in the northeast Atlantic Ocean. *J. Geophys. Res.: Oceans* 100, 6633–6643. <http://dx.doi.org/10.1029/94JC01127>.
- Martin, P., Lampitt, R.S., Jane Perry, M., Sanders, R., Lee, C., D'Asaro, E., 2011. Export and mesopelagic particle flux during a North Atlantic spring diatom bloom. *Deep Sea Res. Part I: Oceanogr. Res. Pap.* 58, 338–349. <http://dx.doi.org/10.1016/j.dsr.2011.01.006>.
- McDonnell, A.M.P., Buesseler, K.O., 2012. A new method for the estimation of sinking particle fluxes from measurements of the particle size distribution, average sinking velocity, and carbon content. *Limnol. Oceanogr. Methods* 10, 329–346.
- McDonnell, A.M.P., Buesseler, K.O., 2010. Variability in the average sinking velocity of marine particles. *Limnol. Oceanogr.* 55, 2085–2096.
- Menden-Deuer, S., Lessard, E.J., 2000. Carbon to volume relationships for dinoflagellates, diatoms, and other protist plankton. *Limnol. Oceanogr.* 45, 569–579.
- Mobley, C.D., 1994. Ch. 3: Optical properties of water, *In* Light and Water, Radiative Transfer in Natural Waters.
- Omand, M.M., D'Asaro, E.A., Lee, C.M., Perry, M.J., Briggs, N., Cetinic, I., Mahadevan, A., 2015. Eddy-driven subduction exports particulate organic carbon from the spring bloom. *Science* 348, 222–225.
- Owens, S.A., Buesseler, K.O., Lamborg, C.H., Valdes, J., Lomas, M.W., Johnson, R.J., Steinberg, D.K., Siegel, D.A., 2013. A new time series of particle export from neutrally buoyant sediment traps at the Bermuda Atlantic Time-series Study site. *Deep Sea Res. Part I: Oceanogr. Res. Pap.* 72, 34–47. <http://dx.doi.org/10.1016/j.dsr.2012.10.011>.
- Resplandy, L., Martin, A.P., Le Moigne, F., Martin, P., Aquilina, A., Mémery, L., Lévy, M., Sanders, R., 2012. How does dynamical spatial variability impact 234Th-derived estimates of organic export? *Deep Sea Res. Part I: Oceanogr. Res. Pap.* 68, 24–45. <http://dx.doi.org/10.1016/j.dsr.2012.05.015>.
- Slade, W.H., Boss, E., Russo, C., 2011. Effects of particle aggregation and disaggregation on their inherent optical properties. *Opt. Express* 19, 7945–7959.
- Siegel, D.A., Buesseler, K.O., Doney, S.C., Salliey, S.F., Behrenfeld, M.J., Boyd, P.W., 2014. Global assessment of ocean carbon export by combining satellite observations and food-web models. *Glob. Biogeochem. Cycles* 28, 181–196. <http://dx.doi.org/10.1002/2013GB004743>.
- Steinberg, D.K., Carlson, C.A., Bates, N.R., Goldthwait, S.A., Madin, L.P., Michaels, A.F., 2000. Zooplankton vertical migration and the active transport of dissolved organic and inorganic carbon in the Sargasso Sea. *Deep Sea Res. Part I: Oceanogr. Res. Pap.* 47, 137–158.
- Turner, J.T., 2002. Zooplankton fecal pellets, marine snow and sinking phytoplankton blooms. *Aquat. Microb. Ecol.* 27, 57–102.
- Turner, J.T., 2015. Zooplankton fecal pellets, marine snow, phytodetritus and the ocean's biological pump. *Prog. Oceanogr.* 130, 205–248. <http://dx.doi.org/10.1016/j.pcean.2014.08.005>.
- Valdes, J.R., Price, J.F., 2000. A neutrally buoyant, upper ocean sediment trap. *J. Atmos. Ocean. Technol.* 17, 62–68. [http://dx.doi.org/10.1175/1520-0426\(2000\)017<0062:ANBUOS>2.0.CO;2](http://dx.doi.org/10.1175/1520-0426(2000)017<0062:ANBUOS>2.0.CO;2).
- van de Hulst, H.C., 1957. *Light Scattering by Small Particles*. John Wiley and Sons, New York.
- Volk, T., Hoffert, M.I., 1985. Ocean carbon pumps: analysis of relative strengths and efficiencies in ocean-driven atmospheric CO₂ changes. In: Sundquist, E.T., Broecker, W.S. (Eds.), *The Carbon Cycle and Atmospheric CO₂: Natural Variations Archean to Present*. American Geophysical Union, 99–110.
- Voss, K.J., Austin, R.W., 1993. Beam-attenuation measurement error due to. *J. Atmos. Ocean. Technol.* 10, 113–121.
- Waterhouse, A.F., MacKinnon, J.A., Nash, J.D., et al., 2014. Global patterns of diapycnal mixing from measurements of the turbulent dissipation rate. *J. Phys. Oceanogr.* 44, 1854–1872. <http://dx.doi.org/10.1175/JPO-D-13-0104.1>.